Highly efficient Cr(VI) removal by cationic covalent organic framework

Xiao-Meng Liu, Yin-Tao Su, Jian-Zhong Guo and Bing Li*

College of Chemistry and Materials Engineering, Zhejiang A&F University, Hangzhou, Zhejiang 311300, P. R. China

Corresponding author: libingzjfc@163.com

GRAPHICAL ABSTRACT

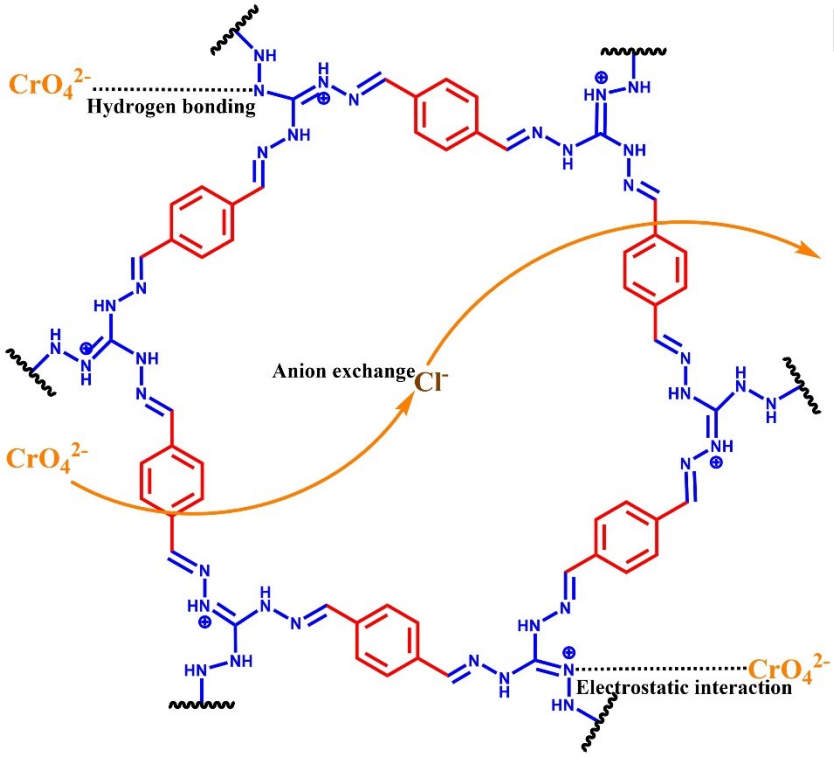

Abstract

Developing an efficient sorbent for removing the highly toxic Cr(VI) is very important, which tackles the threat of Cr(VI) pollution to ecological environment and human health. Herein, a cationic covalent organic framework bearing cationic guanidine (named $TATG_{Cl}$) was synthesized from terephthalaldehyde (TA) and

triaminoguanidinium chloride (TG_{Cl}), and exploited to discard Cr(VI) from water. The Cr(VI) removal ability of $TATG_{Cl}$ strongly relies on the aqueous pH, and is strong at low pH. The removing ability is obviously also affected by ionic strength. The Cr(VI) sorption process on $TATG_{Cl}$ obeys pseudo-second-order and Langmuir models. Batch adsorption experiments and characterization show that the guanidine group on the skeleton of $TATG_{Cl}$ is pivotal in capturing Cr(VI) through hydrogen bonding and anion exchange/electrostatic interaction. A reduction mechanism also exists in the Cr(VI) disposal by a small amount of unreacted aldehyde group of $TATG_{Cl}$. The large removal ability makes $TATG_{Cl}$ a prospective candidate for discarding Cr(VI) from water.

Keywords: Cr(VI); Removal; Adsorption; Covalent organic framework

Introduction

Excessive emission of poisonous heavy metals from diverse industrial fields is one major ecological concern. Especially, hexavalent chromium (Cr(VI)), which exists as $Cr_2O_7^{2-}$, $HCrO_4^-$, or CrO_4^{2-} in water, is a frequent pollutant in groundwater and surface water because of its extensive application in pigment, electroplating and other industries. Cr(VI) is a highly toxic pollutant (Thompson et al. 2022; Ma et al. 2022). Once the water body or drinking water source is contaminated by Cr(VI), it will severely threaten human health. The World Health Organization has set a strict upper limit of 50 $\mu g \cdot L^{-1}$ Cr(VI) in drinking water. Hence, Cr(VI) shall be urgently discarded from polluted water media to meet the emission standard. Recently, diverse Cr(VI) disposing methods from polluted water are developed, including adsorption, membrane

filtration, and reduction-precipitation (Zhu et al. 2020; Wang et al. 2022; Putra-Hidayat et al. 2022; Guo et al. 2020). Adsorption is a feasible method with low cost, convenience, simplicity and effectiveness in Cr(VI) removal. Currently, many materials including hydrochar, biochar, metal-organic frameworks (MOFs), and zeolite are developed to address Cr(VI) (Zhang et al. 2022; Li et al. 2021a; Daradmare et al. 2021). Various adsorption materials have pros and cons for different pollutants. Therefore, it is significant and challenging to develop new efficient adsorbents.

Covalent organic frameworks (COFs), a novel type of porous materials, have low density, large specific surface area, permanent porocity, and acceptable chemical stability (Martinez-Bulit et al. 2022; Jiang et al. 2020; Mitra et al. 2016). In the last ten years, COFs with discrepant structures and performances are produced by formulating accurate building blocks of the molecular frame and used in extensive fields in catalysis, adsorption/separation, and biomedicine (Gendy et al. 2022; Deng et al. 2021a; Garai et al. 2021). COFs are prospective candidates for Cr(VI) pollution remediation, but their structures for Cr(VI) adsorption are very limited and their prices are relatively high. For example, Cui et al. synthesized dual-pore COF-BTA-DHBZ from concentration of 3,3'-dihydroxybenzidine and 1,1′-biphenyl-3,3′,5,5′-tetracarbaldehyde, where the –OH in the pores of COF–BTA–DHBZ was pivotal in catching Cr(VI) (Cui et al. 2019).

Cationic COFs (cCOFs) are a less-explored subgroup of COFs with electrostatic activity, and are composed of cationic organic units and weakly-bonded anions in pores or interlayers. cCOFs can be accurately aggregated by monomers that contain pre-designed ion sites (Da et al. 2019; He et al. 2019; Liang et al. 2022).

Triaminoguanidinium chloride (TG_{Cl}) with positive charge, rich nitrogen and low cost is an ideal monomer to synthesize cCOFs for adsorbing anionic pollutants.

Herein, an $TATG_{Cl}$ with cationic guanidine groups was feasibly prepared from inexpensive terephthalaldehyde (TA) and TG_{Cl} for efficiently removing Cr(VI). The Cr(VI) removing ability of $TATG_{Cl}$ was studied by batch tests and characterized by various techniques. The possible removal mechanism between $TATG_{Cl}$ and Cr(VI) was analyzed by FTIR and XPS.

2. Materials and methods

2. 1 Materials

TA, ethanol, acetic acid, guanidine hydrochloride (GH), hydrazine hydrate (80%), 1,4-dioxane, and potassium dichromate of analytical purity were made in Sinopharm (Shanghai) Chemical Reagent Co., Ltd..

2.2 Synthesis of cationic $TATG_{Cl}$

TG_{Cl} was produced from reaction of GH (20 mmol), hydrazine hydrate (80%, 3.5 mL) and 1,4-dioxane (10 mL) at 100 °C for 3 h (Sheng et al. 2022).

$TATG_{Cl}$ was prepared by Schiff reaction between TA and TG_{Cl} in a solvothermal way (Scheme 1). Briefly, TA (36 mmol) and TG_{Cl} (24 mmol) were dispersed into a blend of water (80 mL), ethanol (240 mL) and 6 $mol \cdot L^{-1}$ acetic acid (30 mL). Then 15 min of sonication was followed by 1-day reaction in a Telfon autoclave at 120 ℃. Brown solids of $TATG_{Cl}$ were harvested by filtering, cleaned with ethanol and DMF,

and dried at 60 °C.

2.3 Characterization

A Nicolet iS50 Fourier transform infrared (FTIR) spectrometer, a Malvern Zetasizer Nano ZS90 zeta potential analyzer and a Bruker D8 Advance powder X-ray diffractometer (PXRD) were used here. Morphology and composition of $TATG_{Cl}$ were observed on an FEI Quanta 400 FEG scanning electron microscope (SEM) and XPS spectrometer (ESCALAB 250Xi). Nitrogen ad-/de-sorption isotherms were recorded on a Micromeritics ASAP 2020 meter at 77 K.

2.4 Sorption experiments

Batch sorption tests involving initial Cr(VI) level, contact time, temperature, pH of solution, and ionic strength were conducted to evaluate the Cr(VI) adsorbing capacity of $TATG_{Cl}$. Generally, 20 mg of $TATG_{Cl}$ was dispersed in 50 mL of a 30 to 300 $mg \cdot L^{-1}$ Cr(VI) solution at pH 2 under a specified temperature (298–308 K) for certain contact time. Then the supernatant was obtained via membrane filtration and the Cr(VI) level after adsorption was detected using a visible spectrophotometer with the diphenylcarbazide method at 540 nm (Zhang et al. 2022). The 100 $mg \cdot L^{-1}$ Cr(VI) solutions were adjusted to pH 1–11 with HCl or NaOH solution to assess the influence of pH on the adsorption ability at 303 K. A 150 $mg \cdot L^{-1}$ Cr(VI) solution was added with 0–0.3.0 $mol \cdot L^{-1}$ Na_2SO_4 to test the effects of ionic strength on the adsorption ability at 298 K. In desorption assays, 0.1 $mol \cdot L^{-1}$ NaOH was used to desorb Cr(VI) from the

preadsorbed $TATG_{Cl}$. Then the desorbed $TATG_{Cl}$ was cleaned with water and dried for reuse.

The adsorbed Cr(VI) quantity by $TATG_{Cl}$ (q_e, $mg \cdot g^{-1}$) was determined as:

$$q_e = (C_o - C_e)V/m$$

where C_o and C_e ($mg \cdot L^{-1}$) are the initial and final Cr(VI) levels, respectively; m is the mass of $TATG_{Cl}$ (g); V is the volume of the Cr(VI) solution (L).

3. Results and discussion

3.1. Characterization

SEM reveals inhomogeneous particles in the morphology of the $TATG_{Cl}$, which are irregularly stacked together by different pieces (Figure 1a). EDS shows the main elements of $TATG_{Cl}$ are C, N and Cl (Figure 1c). After adsorption of Cr(VI), the SEM image does not change significantly, implying $TATG_{Cl}$ is stable in aqueous solutions (Figure 1b). On the EDS images, the Cr element appears, but the Cl element is absent, suggesting Cr ions are adsorbed onto the surface of $TATG_{Cl}$, and ion exchange is involved in the adsorption (Figure 1d) (Zhang et al. 2022).

The N_2 ad-/de-sorption isotherms of $TATG_{Cl}$ at 77 K show a II adsorption model and the main pore size is 27 nm (Liang et al. 2022) (Figure 2a). The pore volume and BET surface area of $TATG_{Cl}$ are 0.04338 $cm^3 \cdot g^{-1}$ and 19.61 $m^2 \cdot g^{-1}$, respectively. The smaller BET surface area of $TATG_{Cl}$ may be because $TATG_{Cl}$ is less crystalline and counterion exists in the pore channels, as identified in $TpTG_{Cl}$, $DhaTG_{Cl}$ and SCU-COF-1 (Wang et al. 2022; Da et al. 2019; He et al. 2019).

The main wide peak at 2θ = ~27° on the PXRD pattern of $TATG_{Cl}$ suggests weak π-π stacking between the vertically-piled 2D layers (Figure 2b). This kind of structure is less-crystalline or amorphous because ordered structures are hindered by the charge repulsion between adjacent layers (Da et al. 2019; He et al. 2019).

FTIR spectra of $TATG_{Cl}$ without and with Cr(VI) adsorption and the corresponding precursors are shown in Figure 3. In the FT-IR spectrum of $TATG_{Cl}$, the new peak at 1632 cm^{-1} reflects C=N stretching vibration, which demonstrates the imine bonding caused by the condensation between the −CHO of TAT and the $-NH_2$ of TG_{Cl} (Jiang et al. 2020). The vanishing typical peaks at 3331 and 3218 cm^{-1} from N−H of TG_{Cl}, and at ~2866 and 1694 cm^{-1} for the aldehyde group of TAT also imply imine bonds are formed from the Schiff reaction (Da et al. 2019).

3.2 Adsorption isotherm of Cr(VI) onto $TATG_{Cl}$

It is very meaningful to describe the adsorption isotherm, which can estimate the maximum adsorption capacity of $TATG_{Cl}$ and uncover the $TATG_{Cl}$ and Cr(VI) interaction. Cr(VI) adsorption isotherms onto $TATG_{Cl}$ were depicted in Figure 4a. The Cr(VI) absorption capacity of $TATG_{Cl}$ was enchanced significantly with the increasing initial concentration at low equilibrium concentrations, and then rose gradually until reaching saturation. The temperature rise facilitated the Cr(VI) removal, but the effect was small, suggesting the removal process was endothermic.

The equilibrium and corresponding parameters fitted using the linearized Langmuir and Freundlich isotherm models were listed in Table 1 (Chen et al. 2019; Li et al. 2018).

The linear relationship of the Langmuir model (C_e/q_e against C_e) (Figure 4b) with higher R^2 was better than the Freundlich model ($\ln q_e$ against $\ln C_e$) (Figure 4c)for Cr(VI) adsorption on $TATG_{Cl}$. Therefore, the Langmuir model is more feasible for explaining the Cr(VI) adsorption on $TATG_{Cl}$, or namely monolayer adsorption. The largest Cr(VI) adsorbing ability on $TATG_{Cl}$ at three temperatures under the experimental conditions is close to the experimental results. $TATG_{Cl}$ outperformed other adsorbents listed in Table 2.

3.3. Sorption kinetics

The Cr(VI) adsorbing kinetics onto $TATG_{Cl}$ was shown in Figure 5a. The Cr(VI) adsorption onto $TATG_{Cl}$ was balanced within 360 min. The process is divided into two evident stages. The rapid Cr(VI) adsorption in the first stage was attributed to the numerous active sites on $TATG_{Cl}$ and plenty aqueous Cr(VI). Then the adsorption amount increased slowly in the second stage until reaching the adsorption equilibrium. This slow adsorption process may come from two aspects. (1) When almost all surface adsorbing sites are taken, Cr(VI) needs certain time to arrive at the interior sites. (2) With the enhanced adsorption capacity, the electrostatic repulsion between the adsorbed Cr(VI) and Cr(VI) in the liquid phase is stronger, resulting in higher resistance against Cr(VI) adsorption. To better understand the Cr(VI) adsorbing behaviour of $TATG_{Cl}$, we simulated the kinetic sorption data using the pseudo-second-order (PSO, t/q_t vs. t) or pseudo-first-order (PFO, $\ln(q_e–q_t)$ vs. t) kinetic models (Figure 5b/5c) (Chen et al. 2019; Li et al. 2018).

The parameters from linear fitting are listed in Table 3. Evidently, the $q_{e,cal}$ computed by the PSO model more agreed with the experimental data ($q_{e,exp}$) than the PFO model, because of the larger correlation coefficient (R^2). The results indicate that the Cr(VI) adsorption of $TATG_{Cl}$ is chemisorption including ion exchange and electrostatic interaction (Figure 6).

3.4. Effects of pH and ionic strength

pH is critical in removing Cr(VI), and impacts the surface charge of the adsorbent and the existing form of Cr(VI). Cr(VI) in water solutions mainly exists as $HCrO_4^-$ at pH < 5, and as CrO_4^{2-} under alkaline conditions from the Pourbaix diagram (Li et al. 2021b; Zhang et al. 2022). The zeta potential of $TATG_{Cl}$ was shown in Figure 7a, and pH of the zero point potential is 5.4. As the pH rose from 2.0 to 11.0, the Cr(VI) adsorption by $TATG_{Cl}$ decreased, and the adsorption capacity was the largest at pH 2.0 (Figure 7a). Thus, low pH facilitates the Cr(VI) removal because the hydrogen bond/electrostatic attraction between cationic $C{=}NH^+$ unit and anionic Cr(VI) species. In addition, $TATG_{Cl}$ can reduce Cr(VI) to Cr(III) in the acidic environment ($HCrO_4^- + 7H^+ + 3e^- \rightarrow Cr^{3+} + 4H_2O$) (Zhang et al. 2022).

To further prove that electrostatic interaction is the key adsorption, we studied the effect of coexisting anions (Figure 7b). Therefore, the effect of Na_2SO_4 on Cr(VI) adsorption was tested. When the Na_2SO_4 concentration rose from 0 to 0.30 $mol \cdot L^{-1}$, the Cr(VI) adsorption capacity dropped significantly from 98.6 to 49.2 $mg \cdot g^{-1}$ due to the competition in the adsorption between $HCrO_4^-$ with SO_4^{2-}, indicating electrostatic

interaction is an important mechanism for $TATG_{Cl}$ to adsorb Cr(VI).

3.5 Adsorption thermodynamics analysis

Generally, thermodynamic parameters are important for assessing the changes during adsorption. The changes in Gibbs free energy (ΔG), enthalpy (ΔH), and entropy (ΔS) were determined by isothermal and van't Hoff equations and the parameters were listed in Table 4 (Li et al. 2021c). The Cr(VI) adsorption on $TATG_{Cl}$ is spontaneous and feasible (ΔG<0) and exothermic (ΔH>0) with an increment in randomness (ΔS <0).

3.6 Removal mechanism

After adsorption of $HCrO_4^-$, the new peaks at 936 and 777 cm^{-1} in the infrared spectrum (Figure 3) reflect the stretched vibration of Cr=O and Cr−O in $TATG_{Cl}$-$HCrO_4^-$. A new broad peak at 3162 cm^{-1} may imply the formation of strong NH···O hydrogen bond between guanidine of $TATG_{Cl}$ and $HCrO_4^-$ (Da et al. 2019). The new peak at 3273 cm^{-1} may be induced by the stretching vibration of −OH in −COOH, indicating the unreacted aldehyde group is oxidized to carboxylic acid during the adsorption.

The XPS spectra showed C, N, O and Cl elements existed in $TATG_{Cl}$ (Figure 8a). Meanwhile, Cr2p peaks appeared and Cl2p peak disappeared in the full-scale XPS spectrum of $TATG_{Cl}$ after adsorption (Figure 8b), confirming chromium ion was successfully bonded on the $TATG_{Cl}$ surface and ion exchange occurred (Zhang et al. 2022).

The peaks on the high-resolution C1s spectrum at 284.8, 285.4 and 287.8 eV can be assigned to C=C, C–N, and C=N/C=O, respectively (Figure 8d) (Deng et al. 2021b). A small new peak at 290.2 eV after the Cr(VI) treatment (Figure 8g) stands for –COOH, implying the little amount of unreacted aldehyde group in $TATG_{Cl}$ was oxidated to carboxylic acid during the adsorption. The O1s peak at 532.5 eV was assigned to the unreacted aldehyde group (Figure 8e). After the capture of Cr(VI), new peaks appeared at 530.2 (Cr–O) and 531.5 eV (C=O/Cr=O) and a peak at 532.7 eV (–COOH) (Figure 8h) (Zhu et al. 2020). The N1s in $TATG_{Cl}$ can be divided into four peaks centered at 398.9, 400.1, 401.0 and 403.6 eV, which reflect C=N, –NH, $C=NH^+$ and N–N, respectively (Figure 8f) (Da et al. 2019). After Cr(VI) adsorption, the binding energy of $C=NH^+$ moved to 401.2 eV due to the electrostatic action between Cr(VI) and $C=NH^+$. Other binding energies of N1s hardly shifted after adsorption, indicating it was not engaged in Cr(VI) adsorption (Figure 8i). The high-resolution Cr2p XPS spectrum showed three peaks at 577.1 587.6, and 579.3 eV, which are ascribed to 2p1/2 and 2p3/2 of Cr(III), and 2p3/2 of Cr(VI) respectively (Figure 8c) (Zhu et al. 2020). This result implies both Cr(VI) and Cr(III) are present in $TATG_{Cl}$, which may be because Cr(VI) was partially reduced to Cr(III) during adsorption. Hence, we think Cr(VI) is partly reduced to Cr(III) in the adsorption, and is caught in the layer channels.

3.7 Regeneration of $TATG_{Cl}$

Since Cr(VI) adsorption on $TATG_{Cl}$ is electrostatic interaction and hydrogen bonding, the aqueous pH affects the surface charge of $TATG_{Cl}$ and the existing form of Cr(VI),

weakening the Cr(VI) adsorbing capacity. Therefore, the adsorbed Cr ions can be eluted with the NaOH solution, and then the $TATG_{Cl}$ can be regenerated with HCl. In the regeneration experiments, the adsorption capacity dropped by only 10% after 5 cycles, so the adsorbent has high regenerability and stability (Figure 9).

4. Conclusions

$TATG_{Cl}$ with cationic guanidine was obtained from the Schiff-base reaction and can strongly eliminate Cr(VI). The guanidine helps $TATG_{Cl}$ perform in eliminating Cr(VI) via electrostatic interaction/ion exchange and hydrogen bonding. According to the Langmuir model, the largest adsorbing ability of $TATG_{Cl}$ is 191.57 $mg \cdot g^{-1}$ at pH 2, a Cr(VI) concentration of 300 $mg \cdot L^{-1}$, and a solid-liquid ratio of 0.4 $g \cdot L^{-1}$ for 12 h. The adsorption mechanism mainly involves hydrogen bonding, anion exchange and electrostatic interaction. Hence, the $TATG_{Cl}$ will be an excellent platform for developing effective adsorbents to discard highly toxic Cr(VI) from wastewater.

Conflict of interest

None.

Acknowledgement

Thanks to the National Natural Science Foundation of China (No. 12175200 and 32271528).

References

Chen, X., Li, B., Shen, Y. and Guo, J.Z. (2019). Facile Synthesis of Calcite-Impregnated Hydrochar with High Sorption Capacity for Cu(II) from Aqueous Solution. *ACS Omega*, 4, 15022−15029.

Cui, F.Z., Liang, R.R., Qi, Q.Y., Jiang, G.F. and Zhao, X. (2019). Efficient Removal of Cr(VI) from Aqueous Solutions by a Dual-Pore Covalent Organic Framework. *Advanced Sustainable Systems*, 3, 1800150.

Da, H.J., Yang, C.X. and Yan, X.P. (2019). Cationic Covalent Organic Nanosheets for Rapid and Selective Capture of Perrhenate: An Analogue of Radioactive Pertechnetate from Aqueous Solution. *Environmental Science & Technology*, 53, 5212−5220.

Daradmare, S., Xia, M., Le, V.N., Kim, J. and Park, B.J. (2021). Metal-organic frameworks/alginate composite beads as effective adsorbents for the removal of hexavalent chromium from aqueous solution. *Chemosphere*, 270, 129487.

Deng, X., Zhao, P., Zhou, X. and Bai, L. (2021a). Excellent sustained-release efficacy of herbicide quinclorac with cationic covalent organic frameworks. *Chemical Engineering Journal*, 405, 126979.

Deng, S.Q., Li, D.M., Mo, X.J., Miao, Y.L., Cai, S.L., Fan, J., Zhang, W.G. and Zheng, S.R. (2021b). Covalent Cross-Linking of Metal-Organic Cages: Formation of an Amorphous Cationic Porous Extended Framework for the Uptake of Oxo-Anions from Water. *ChemPlusChem*, 86, 696−696.

Garai, B., Shetty, D., Skorjanc, T., Gándara, F., Naleem, N., Varghese, S., Sharma, S.K.,

Baias, M., Jagannathan, R., Olson, M.A., Kirmizialtin, S. and Trabolsi, A. (2021). Taming the Topology of Calix[4]arene-Based 2D-Covalent Organic Frameworks: Interpenetrated vs Noninterpenetrated Frameworks and Their Selective Removal of Cationic Dyes. *Journal of the American Chemical Society*, 143, 3407−3415.

Gendy, E.A., Oyekunle, D.T., Ifthikar, J., Jawad, A. and Chen, Z. (2022). A review on the adsorption mechanism of different organic contaminants by covalent organic framework (COF) from the aquatic environment. *Environmental Science and Pollution Research*, 29, 32566–32593.

Guo, J.Z., Xu, H., Chen, L., and Li, B. (2022). A pyridinium functionalization chitosan for efficient elimination of methyl orange and Cr(VI). *Bioresource Technology*, 365, 128112.

He, L., Liu, S., Chen, L., Dai, X., Li, J., Zhang, M., Ma, F., Zhang, C., Yang, Z., Zhou, R., Chai, Z. and Wang, S. (2019). Mechanism unravelling for ultrafast and selective $^{99}TcO_4^-$ uptake by a radiation-resistant cationic covalent organic framework: a combined radiological experiment and molecular dynamics simulation study. *Chemical Science*, 10, 4293–4305.

Jiang, W., Peng, D., Cui, W.R., Liang, R.P. and Qiu, J.D. (2020). Charge-Enhanced Separation of Organic Pollutants in Water by Anionic Covalent Organic Frameworks. *ACS Omega* 5, 32002−32010.

Jia, D., Jing, Z., Duan, Y. and Li, J. (2022). Ultrafast removal of Cr(VI) ions using polyamine modified carbon nanotubes. *Journal of the Taiwan Institute of Chemical Engineers*, 133, 104265.

Li, B., Wang, Q., Guo, J.Z., Huan, W.W., Liu, L. (2018). Sorption of methyl orange from aqueous solution by protonated amine modified hydrochar. *Bioresource Technology*, 268, 454–459.

Liang, J., Chen, Y., Cai, M., Gan, M. and Zhu, J. (2021). One-pot pyrolysis of metal-embedded biochar derived from invasive plant for efficient Cr(VI) removal. *Journal of Environmental Chemical Engineering*, 9, 105714.

Liang, Y., Xia, M., Yu, Q., Li, Y., Sui, Z., Yuan, Y., Hu, X.M., Chen, Q. and Wang, N. (2022). Guanidinium-based ionic covalent organic frameworks for capture of uranyl tricarbonate. *Advanced Composites and Hybrid Materials*, 5, 184–194.

Li, S.Y., Teng, H.J., Guo, J.Z., Wang, Y.X. and Li, B. (2021a). Enhanced removal of Cr(VI) by nitrogen-doped hydrochar prepared from bamboo and ammonium chloride. *Bioresource Technology*, 342, 126028.

Li, Y.X., Han, Y.C. and Wang, C.C. (2021b). Fabrication strategies and Cr(VI) elimination activities of the MOF derivatives and their composites. *Chemical Engineering Journal*, 405, 126648.

Li, H.Z., Zhang, Y.N., Guo, J.Z., Lv, J.Q., Huan, W.W., Li, B. (2021c). Preparation of hydrochar with high adsorption performance for methylene blue by co-hydrothermal carbonization of polyvinyl chloride and bamboo. *Bioresource Technology*, 337, 25442.

Ma, Y., Li, S., Ye, S., Hu, D., Wei, L. and Xiao, F. (2022). Hexavalent chromium triggers hepatocytes premature senescence via the GATA4/NF-κB signaling pathway

mediated by the DNA damage response. *Ecotoxicology and Environmental Safety*, 239, 113645.

Martinez-Bulit, P., Sorrenti, A., Miguel, D.R.S., Mattera, M., Belce, Y., Xia, Y., Ma, S., Huang, M.H., Pané, S. and Puigmartí-Luis, J. (2022). In flow-based technologies: A new paradigm for the synthesis and processing of covalent-organic frameworks, *Chemical Engineering Journal*, 435,135117.

Mitra, S., Kandambeth, S., Biswal, B.P., Khayum A.M., Choudhury, C. K., Mehta, M., Kaur, G., Banerjee, S., Prabhune, A., Verma, S., Roy, S., Kharul, U. K. and Banerjee, R. 2016 Self-Exfoliated Guanidinium-Based Ionic Covalent Organic Nanosheets (iCONs). *Journal of the American Chemical Society*, 138, 2823−2828.

Putra-Hidayat, A.R., Widyanto, A.R., Asranudin, A., Ediati, R., Sulistiono, D.O., Putro, H.S., Sugiarso, D., Prasetyoko, D. , Purnomo, A.S., Bahruji, H., Alia, B.T.I. and Caralina, I.S. (2022). Recent development of double chamber microbial fuel cell for hexavalent chromium waste removal. *Journal of Environmental Chemical Engineering*, 10, 107505.

Qu, J., Liu, Y., Meng, J., Bi, F., Ma, S., Zhang, G., Wang, Y., Tao, Y., Jiang, Z. and Zhang, Y. (2022). Pinecone-derived magnetic porous hydrochar co-activated by $KHCO_3$ and K_2FeO_4 for Cr(VI) and anthracene removal from water. *Environmental Pollution*, 306, 119457.

Thompson C.M., Aardema, M.J., Heintz, M.M., MacGregor, J.T., and Young, R.R. (2022). A review of mammalian in vivo genotoxicity of hexavalent chromium: implications for oral carcinogenicity risk assessment. *Critical Reviews in Toxicology*,

51 (10), 820-849.

Wang, C.C., Ren, X.Y., Wang, P. and Chang, C. (2022). The state of the art review on photocatalytic Cr(VI) reduction over MOFs-based photocatalysts: From batch experiment to continuous operation. *Chemosphere* 303, 134949.

Sheng, F., Li, X., Li, Y., Afsar, N. U., Zhao, Z., Ge, L. and Xu, T. (2022). Cationic covalent organic framework membranes for efficient dye/salt separation. *Journal of Membrane Science***,** 644, 120118.

Xie, H., Wan, Y., Chen, H., Xiong, G., Wang, L., Xu, Q., Li, X. and Zhou, Q. (2021). Cr(VI) Adsorption from Aqueous Solution by UiO-66 Modified Corncob. Sustainability, 13, 12962.

Zhang, Y.N., Guo, J.Z., Wu, C., Huan, W.W., Chen, L. and Li, B. (2022). Enhanced removal of Cr(VI) by cation functionalized bamboo hydrochar. *Bioresource Technology*, 347, 126703.

Zeng, H. Hu, Z., Peng, C., Deng, L. and Liu, S. (2021). Effective Adsorption and Sensitive Detection of Cr(VI) by Chitosan/Cellulose Nanocrystals Grafted with Carbon Dots Composite Hydrogel. *Polymers*, 13, 3788.

Zhu, D., Zhou, S., Zhou, Z., Li, R., Jia, Y., Xu, Z., Lan, S., Zhang, Y., Miao, S. and Wang, W. (2020). Highly efficient and selective removal of Cr(VI) by covalent organic frameworks: Structure, performance and mechanism. *Colloids and Surfaces A*, 600, 124910.

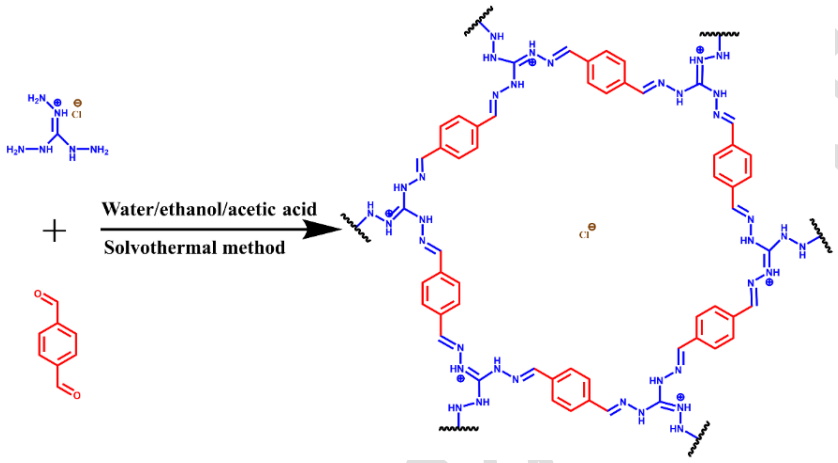

Scheme 1 Synthetic scheme of cationic $TATG_{Cl}$.

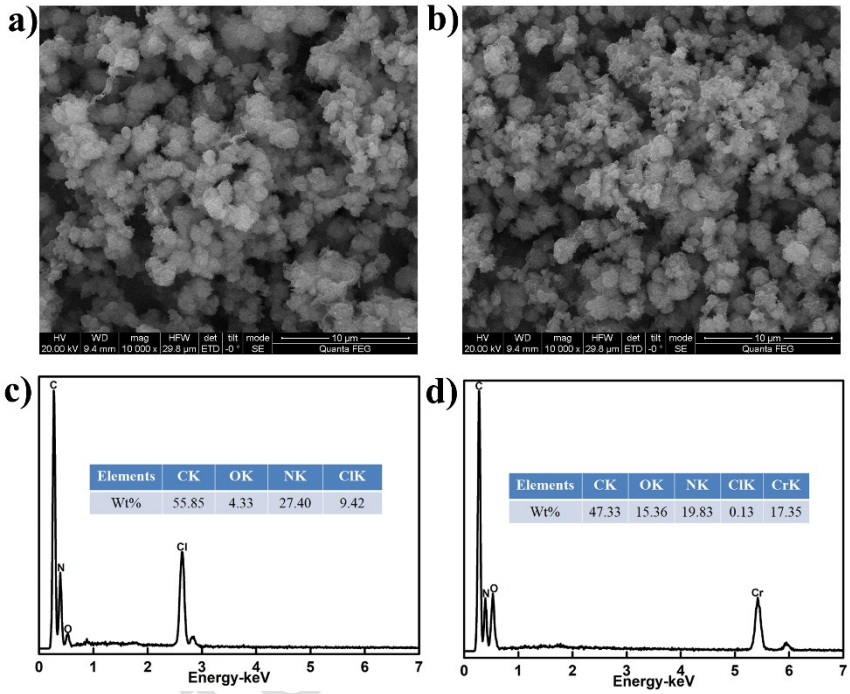

Figure 1 SEM/EDS images of $TATG_{Cl}$ (a/c) and $TATG_{Cl}$ with Cr(VI) (b/d).

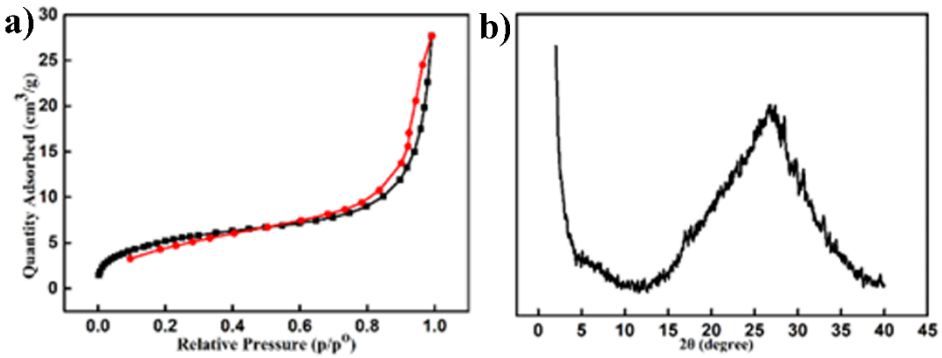

Figure 2 (a) Nitrogen adsorption isotherm of $TATG_{Cl}$. (b) PXRD pattern of $TATG_{Cl}$.

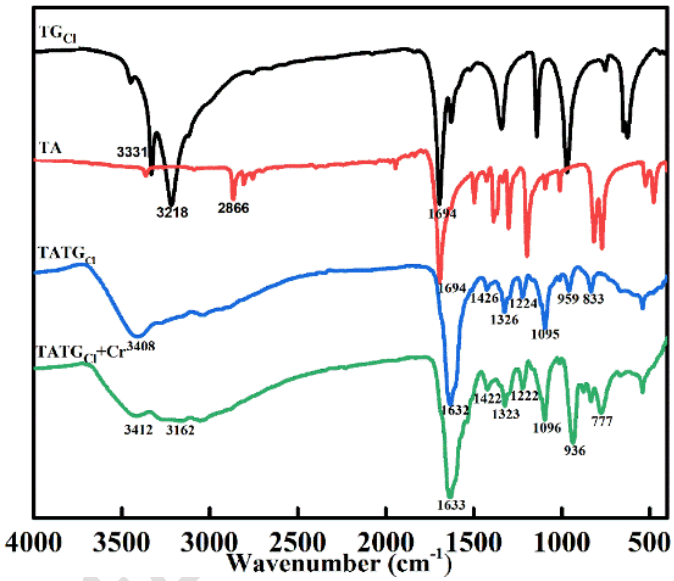

Figure 3 FT-IR spectra of samples.

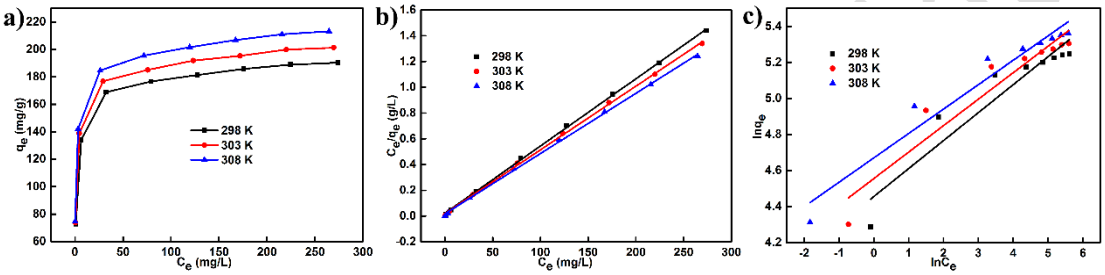

Figure 4 (a) Adsorption isotherms of Cr(VI) on $TATG_{Cl}$. Linearized fitting plots of Langmuir (b) and Freundlich (c) models.

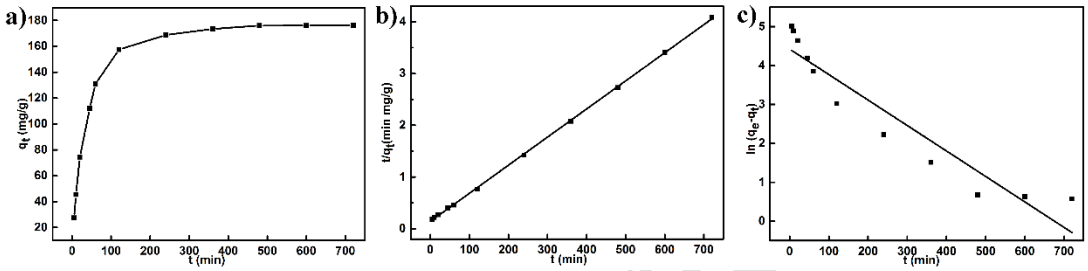

Figure 5 Effect of contact time on Cr(VI) removal by $TATG_{Cl}$. The linearized fitting plots of the PSO (b) and PFO (c) kinetic models.

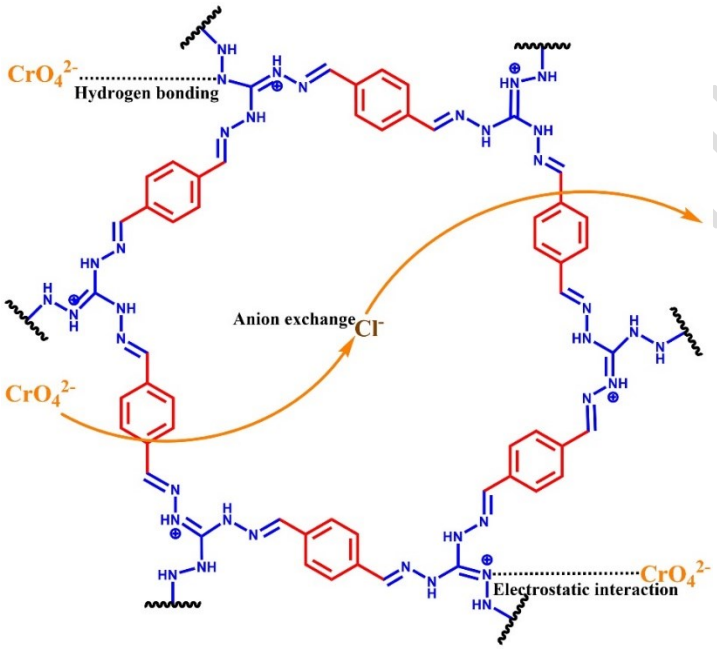

Figure 6 Possible removal mechanism of Cr(VI) on $TATG_{Cl}$.

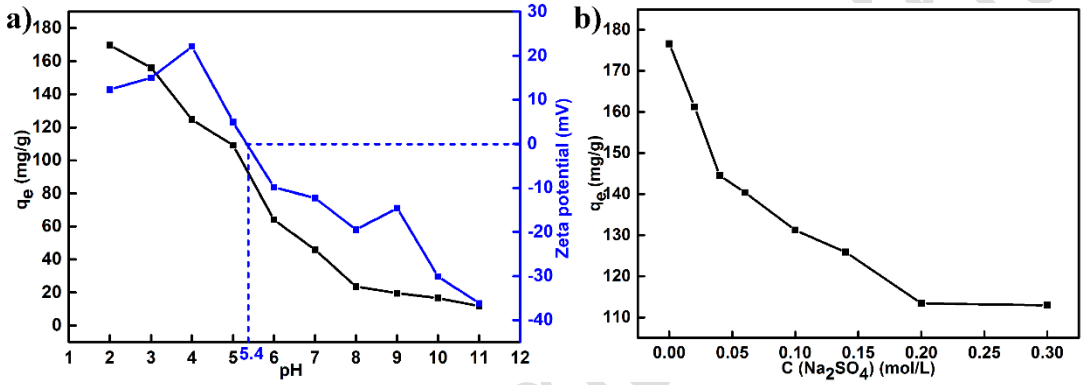

Figure 7 Effects of (a) pH and (b) ionic strength on adsorption.

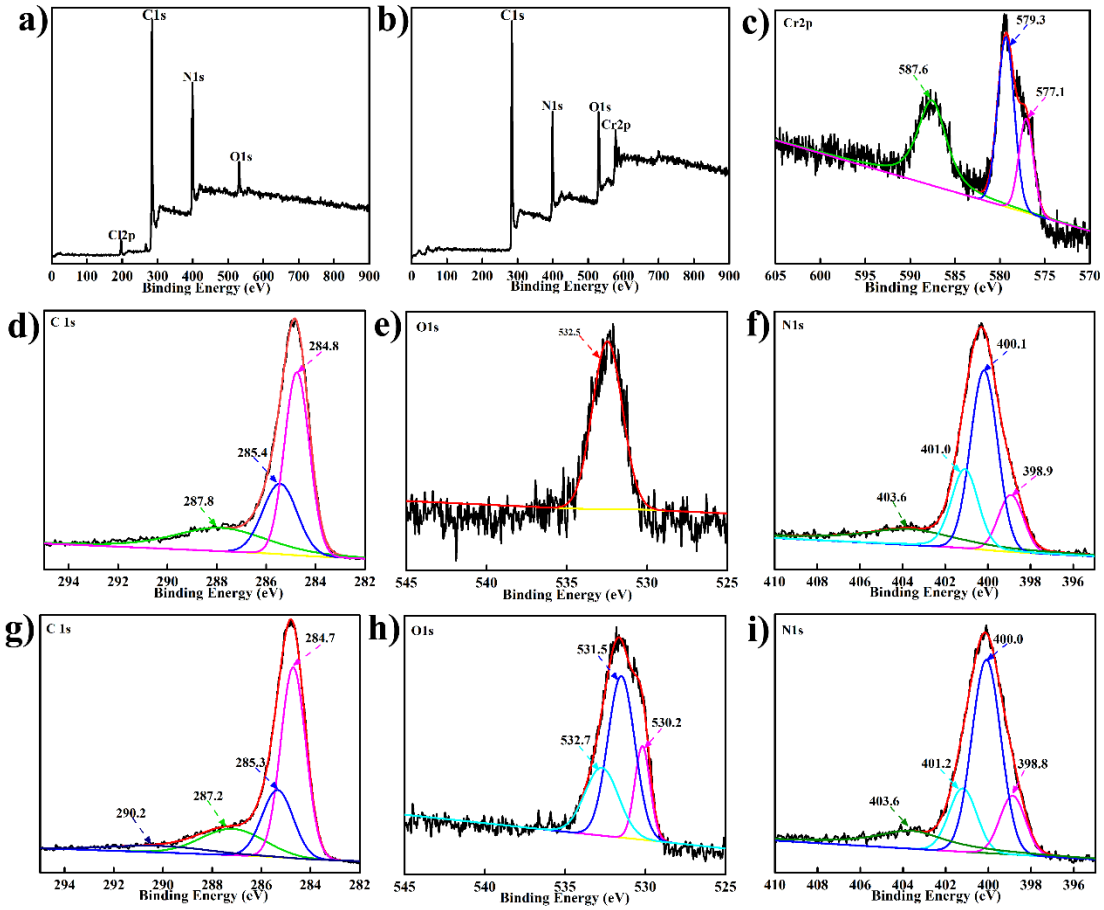

Figure 8 (a) Cl 2p, (b) Cr 2p, and (c) C 1 s XPS spectra of Tp-DGCl and Tp-DGCr

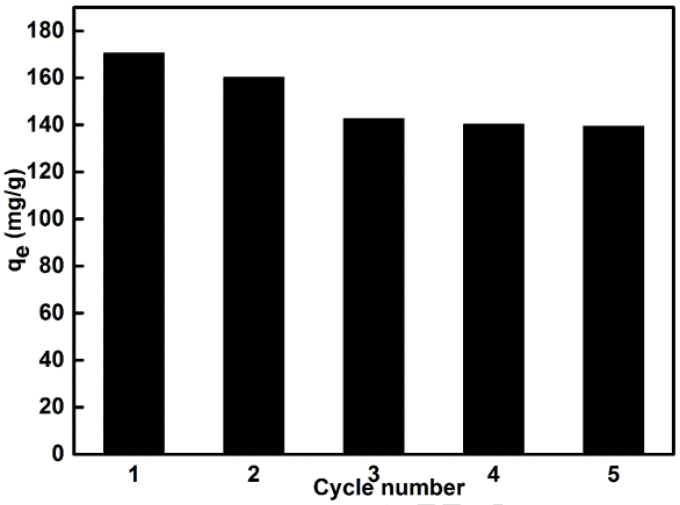

Figure 9 Removal capacity of Cr(VI) by $TATG_{Cl}$ for five successive adsorption cycles.

Table 1 Langmuir and Freundlich parameters for Cr(VI) removal onto $TATG_{Cl}$.

		Langmuir model			Freundlich model		
T(K)	$q_e(exp)$	Q_o (mg·g^{-1})	K_L (L·mg^{-1})	R^2	K_F (mg$^{1-1/n}$·L$^{1/n}$·g^{-1})	*1/n*	R^2
298	190.25	191.57	0.2420	0.99949	86.09	0.15521	0.88043
303	201.23	202.02	0.2619	0.99930	95.09	0.14692	0.89781
308	213.24	213.68	0.2776	0.99915	106.68	0.13544	0.93862

Table 2 Comparison of Cr(VI) adsorption capacity among various materials.

Adsorbent	q_{max} (mg/g)	Reference
UiO-66@Corn^{+}	90.04	Xie et al. 2021
PA-CNTs	168.54	Jia et al. 2022
Chitosan/cellulose nanocrystals loaded with carbon dots	217.8	Zeng et al. 2021
Fe-BC500	47.72	Liang et al. 2021
MPHCMW	128.15	Qu et al. 2022
$TATG_{Cl}$	191.57	This study

Table 3 Kinetic parameters for Cr(VI) adsorption onto $TATG_{Cl}$

PFO model				PSO model		
$q_{e,\,exp}$	$q_{e,\,cal}$	k_1	R^2	$q_{e,cal}$	k_2	R^2
$mg \cdot g^{-1}$	$mg \cdot g^{-1}$	min^{-1}		$mg \cdot g^{-1}$	$mg \cdot g^{-1} \cdot min^{-1}$	
176.23	83.27	0.00654	0.89442	184.16	2.073×10^{-4}	0.99972

Table 4. Thermodynamic values of adsorption of Cr (VI) over $TATG_{Cl}$

Temp. (K)	ΔG (kJ·mol^{-1})	ΔH (kJ·mol^{-1})	ΔS (J·mol^{-1}·K^{-1})	R^2
298	–23.74			
303	–24.34	10.48	114.87	0.98793
308	–24.89			